J. Fluid Mech. (1984), *vol.* 148, *pp.* 207–224
Printed in Great Britain

Turbulent mixing in a pulsed plasma-jet exhaust

By D. R. TOPHAM,
Institute of Ocean Sciences, P.O. Box 6000, Sidney, British Columbia, Canada V8L 4B2

R. M. CLEMENTS
Department of Physics, University of Victoria, British Columbia, Canada V8W 2Y2

AND P. R. SMY
Department of Electrical Engineering, University of Alberta,
Edmonton, Alberta, Canada T6G 2G7

(Received 21 January 1982 and in revised form 3 April 1984)

High-speed schlieren cinéphotography of the firing of a high-energy plasma-jet igniter reveal turbulent structures similar in appearance to laboratory models of thermals or turbulent puffs. Measurements of the growth rates of these features together with those of their impulse and thermal energy confirm this similarity. A simple model based on the entrainment assumption gives a good description of the motion of the element and also of the decay of the internal temperature.

1. Introduction

Recent research into high-energy internal-combustion engine ignition systems has led to the development of the plasma-jet igniter. Typical of such systems is that described by Topham, Smy & Clements (1975), in which approximately 3 J of energy are discharged into a small cylindrical cavity over a period of 30 μs. The resulting plasma is expelled from the cavity as a quasi-steady supersonic jet, and when viewed by eye appears as a bright luminous core about 1 cm in length. Measurements of the ignition characteristics of such devices (Zhang, Clements & Smy 1982) show a time interval of the order of a millisecond between the cessation of the luminous jet and the onset of detectable combustion. It is thus of some interest to enquire into the rate of cooling of the igniter exhaust in this intervening period.

The fluid mechanics of the system can be divided into two distinct phases; a jet flow which accompanies the current discharge, followed by a turbulent mixing stage, with the latter persisting for many times the discharge time. Various aspects of the igniter operation have been described by Topham *et al.* (1975), Oved *et al.* (1979), Cetegen *et al.* (1980), Grant, Marram & McIlwain (1983), Clements, Smy & Dale (1981) and Smy *et al.* (1982, 1983). None of these papers discuss the overall behaviour of the jet, and the results will be reviewed here in the context of mixing during the various phases.

Topham *et al.* (1982) have shown that, during the later stages, the ejected gas takes on the appearance of an isolated turbulent element or 'puff'. The motion of such elements, deduced on a statistical basis from single-frame photographs of many events, was shown to follow the similarity laws for non-buoyant turbulent puffs (Grigg & Stewart 1962; Richards 1965). In the following, we present the results of more detailed studies of the ensuing motion together with a simple model which predicts dilution rates. This shows that, over the period of the ignition delay, mixing has

reduced the mean puff temperature to within a few tens of degrees of the ambient temperature. This rapid cooling is confirmed by interferometer measurements taken within the puff.

2. The initial discharge period

On firing the discharge, an almost spherical shock wave is generated at the cavity exit, followed by a supersonic jet of highly luminous plasma penetrating into the surrounding atmosphere. Figure 1 is a composite photograph illustrating some aspects of this penetration phase. Of the various components, which were taken on different occasions, parts (*a*), (*b*) and (*c*) have been enlarged to a similar scale for ease of comparison. Figure 1 (*a*) is a streak photograph of the luminous region, the slope of the front giving the penetration velocity, which is constant during the discharge period. The curved banded structure running almost parallel to the time axis marks positions of the Mach disks within the supersonic jet. The striations running almost normal to the shock bands arise from variations in the jet luminosity and probably have their origin in arc instabilities. Their slopes are indicative of the local flow speed (typically 5×10^3 m/s, compared with the frontal velocity of 5×10^2 m/s) as demonstrated by Smy *et al.* (1982), and the velocity changes across the shock bands can be discerned on the original photograph. Figure 1 (*b*) is a sequence of submicrosecond exposure photographs taken with an image-converter camera. These show something of the shock structure, and also that the shape of the advancing front is somewhat unstable, sometimes having a forked appearance. An example from a corresponding series of photographs taken with a ruby-laser schlieren system (figure 1 *c*) shows the shock wave, and behind this the outer extremities of the jet flow. In contrast with the narrow luminous jet, the outermost regions of the flow have the appearance of a blunted cone with its base lying in the plane of the cavity exit. The overall appearance of these schlieren pictures is one of a turbulent mixing zone.

These observed flow features follow the general pattern described in jet penetration studies, for example those detailed by Hopkins & Robertson (1967) for the two-dimensional case. Figure 2 is an example of a flow pattern calculated in their paper. The front of the jet is marked by an advancing stagnation point, the original jet fluid behind this dividing to form a shell whose outer extent is marked by a dividing streamline and bounded on the inside by a free streamline, a continuation of the jet boundary.

The figure is drawn in a frame of reference moving with the stagnation point, whose velocity of advance V is in our case identified with the slope of the luminous front of figure 1 (*a*). For constant-density flows the geometry of the streamline pattern is determined by the ratio of the jet velocity in the reference frame to the counterflow, or stagnation-point advance velocity, defined in the notation of Hopkins & Robertson as K. If, as is the case of the plasma jet, the fluids in the two regions are of different densities, the streamline pattern for a given value of K is unchanged, but the required counterflow velocity is scaled by the square root of the density ratio. This follows from the condition that there be no pressure difference across the dividing streamline, and as a consequence a discontinuity in the tangential velocity component occurs.

We believe that the somewhat irregular shape of the frontal region of the jet shown in figure 1 (*b*) is characteristic of a moving stagnation point and that the abrupt quenching of the luminosity is indicative of rapid mixing. The temperature measurements of about 3000 K taken close to the maximum penetration distance (Topham *et al.* 1975) indicate density ratios of about 10, and large velocity differences would

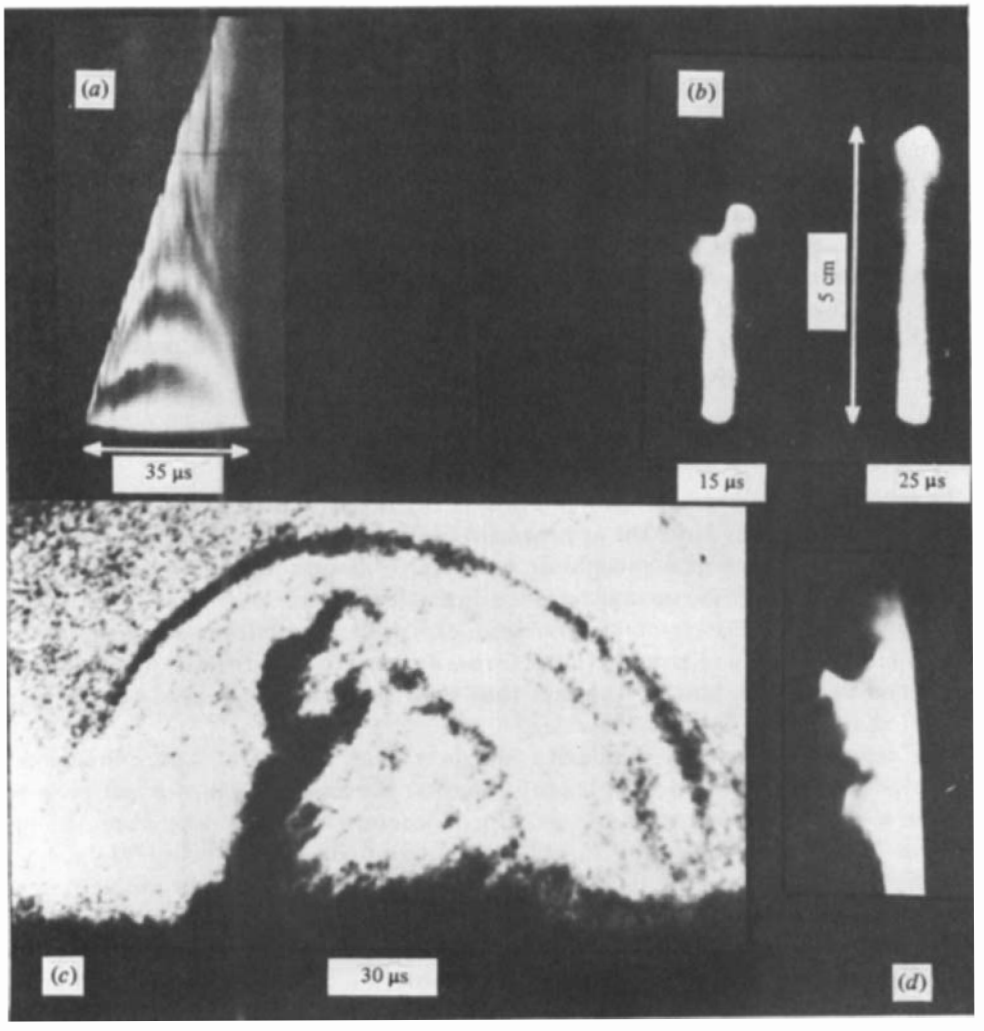

FIGURE 1. Jet phenomena during the discharge period. (*b*) is from Topham *et al.* (1975), and (*c*) is from Oved *et al.* (1979), reproduced with permission.

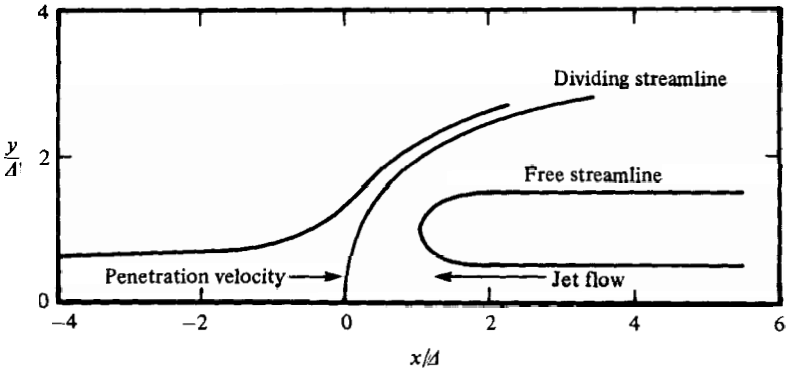

FIGURE 2. Flow pattern of two-dimensional penetrating jet of half-width Δ; after Hopkins & Robertson (1967).

be generated as the flow accelerates away from the stagnation point. This is confirmed by the general appearance of the schlieren photographs of the outer envelope of the flow. Further evidence for turbulent mixing during this phase is offered by figure 1 (*d*), a time exposure of part of the outer regions, the brighter core of the jet having been masked to prevent overexposure. This clearly shows the structure typical of turbulent mixing zones. The clarity of the picture, an integrated time exposure, suggests that the structures in the outer regions move relatively slowly in a frame of reference fixed in the laboratory, as would be expected from the model of Hopkins & Robertson.

If, as we suggest, the region of the dividing streamline is also one of intense mixing, the hot plasma will be diluted and cooled to at least the point of nonluminosity within the timescale of the jet transit time after the cessation of the discharge, or about 5 μs. The fluid contained within the conical region and its circulation patterns form the initial stages of the later turbulent mixing phase.

3. The final mixing stage

Figure 3 shows a series of schlieren photographs taken from a high-speed ciné film of the jet firings. They have the appearance typical of small elements of buoyant fluid in laboratory studies of atmospheric convective clouds (e.g. Turner 1973; Scorer 1978), and exhibit strong geometrical similarity from frame to frame. The short timescales over which these elements have been observed, about 10 ms, suggests that, for the time of interest here, gravitational forces are unimportant to the motion, which is confirmed to some extent by the fact that their behaviour appeared to be independent of the orientation of the device.

The strong geometrical similarity suggests that to a first approximation the elements can be described by a model based on the assumption of a self-preserving flow, in a similar manner to thermals. The characteristic scales depend on the initial impulse I_0, the added enthalpy H_0 and the ambient conditions, being $(H_0/\rho_2 h_2)^{\frac{1}{3}}$ and $I_0 h_2/H_0$ for length and velocity respectively, where ρ_2 and h_2 are the ambient density and enthalpy. For times long enough for mixing to have reduced their density close to ambient, their behaviour should approach that of the neutral-density puffs studied by Grigg & Stewart (1962) and Richards (1965).

An account of the behaviour of the thermals of large initial density difference has been given by Escoudier & Maxworthy (1973), in which they point out the importance of the virtual inertia for accelerated motions and include it in their analysis. Here we adapt their model to gravity-free motions having an initial impulse, and compare the model behaviour with our measurements.

The model is based on the entrainment hypothesis of Morton, Taylor & Turner (1956) applied to a spherical element. The kinematics of such flows have been described by Turner (1964) in the case of a spherical vortex. The assumptions are equivalent to those discussed by Escoudier & Maxworthy as follows:

(i) there is no loss of impulse or heat to a wake;

(ii) the thermal has a spherical shape with uniformly distributed fluid properties;

(iii) the mixing takes place at constant pressure and the gas is assumed to be perfect;

(iv) ambient fluid is entrained into the thermal at a rate proportional to its velocity and surface area. The constant of proportionality α is fixed for a given event, but can vary from one event to another.

To justify the last assumption, Escudier & Maxworthy invoke the experimental evidence of a constant value of α for a given thermal. In the case of the turbulent

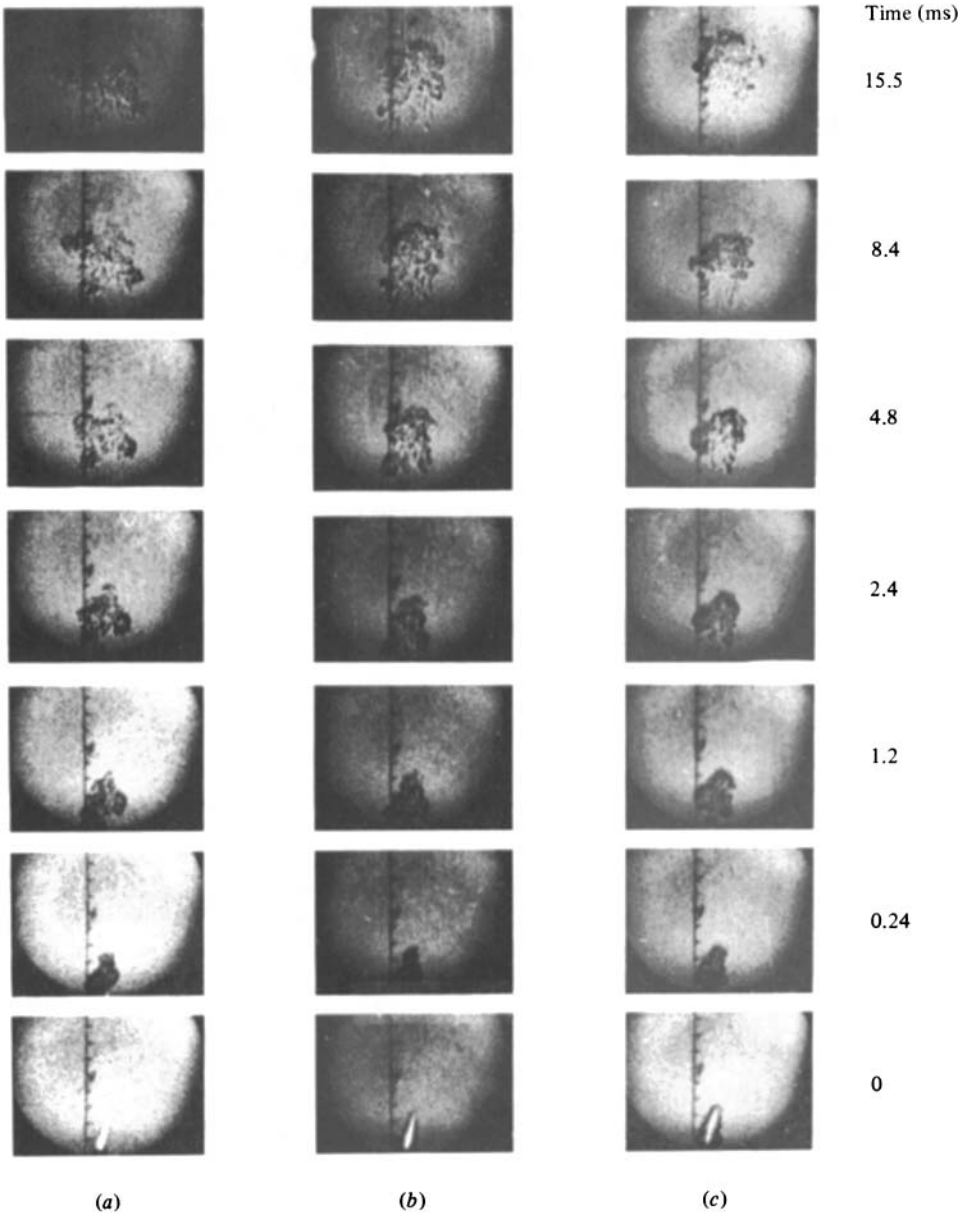

FIGURE 3. Schlieren photography of the mixing elements for the high-energy case: (*a*) discarded; (*b*) run 5; (*c*) run 8.

elements described here, although there is similarity over short times, a detailed examination of their behaviour reveals a slow evolution of forms over long times. To eliminate the effect of these slow changes in form from the analysis of the experiments, the actual puff geometries have been replaced by equivalent spherical elements of the same volume.

Before analysing the non-buoyant puff model in detail, we will examine the momentum equation to determine the relative importance of the buoyancy terms.

Following Escudier & Maxworthy, the appropriate form of the momentum equation can be written as

$$\frac{4\pi}{3}\frac{\mathrm{d}}{\mathrm{d}t}[b^3(\rho_1+k\rho_2)w] = \frac{4\pi}{3}b^3(\rho_2-\rho_1)g, \tag{1}$$

where ρ_1 is the internal density, b the radius, k the virtual-mass coefficient and w the translational velocity. The correct value for k for entraining elements is not known precisely, but in common with other writers we will assume that it is close to that for a solid body of the same instantaneous shape. The right-hand side is the total buoyancy which is conserved during the motion, and hence the equation can be integrated directly to give

$$w = \frac{1-\beta}{\beta+k}gt + \frac{3I_0}{4\pi b^3\rho_2(\beta+k)}, \tag{2}$$

where I_0 is the initial impulse and $\beta \equiv \rho_1/\rho_2$. Under conditions typical of our experiments, $t \sim 10^{-2}$ s, $b \sim 10^{-2}$ m, $\beta \sim 0.5$, $I_0 \sim 10^{-5}$ kg m/s and for a sphere $k = 0.5$. With these numerical values the ratio of the gravity term to the inertia term is of order 10^{-2} and our neglect of gravitational effects can be justified.

The conservation equations for the non-buoyant spherical element then take the form

mass
$$\frac{\mathrm{d}}{\mathrm{d}t}(\rho_1 b^3) = 3\alpha\rho_2 b^2 w, \tag{3}$$

momentum
$$\frac{4\pi}{3}b^3 w(\rho_1+k\rho_2) = I_0, \tag{4}$$

energy
$$\frac{4\pi}{3}b^3\rho_1(h_1-h_2) = H_0, \tag{5}$$

where ρ_1 and h_1 are the internal density and enthalpy respectively.

Writing $\beta \equiv \rho_1/\rho_2$, (5) takes the non-dimensional form

$$b^* = (1-\beta)^{-\frac{1}{3}}, \tag{6}$$

where
$$b^* = b\left(\frac{4\pi\rho_2 h_2}{3H_0}\right)^{\frac{1}{3}}.$$

Substituting for b^2W and b from (4) and (5) into (3) and putting $x \equiv \beta/(1-\beta)$, the following nondimensional differential equation is obtained:

$$\frac{\mathrm{d}x}{\mathrm{d}t^*} = 3\alpha\frac{(1+x)^{\frac{2}{3}}}{(1+k)x+k}, \tag{7}$$

where
$$t^* = t\left(\frac{4\pi}{3}\right)^{\frac{1}{3}}\left[\frac{\rho_2 h_2}{H_0}\right]^{\frac{4}{3}}\frac{I_0}{\rho_2}.$$

At the start of the motion the internal density is taken to be zero, giving the boundary condition $x = 0$ at $t^* = 0$. Equation (7) can then be integrated to give

$$\alpha t^* = \tfrac{1}{4}(1+k)(1+x)^{\frac{4}{3}} - (1+x)^{\frac{1}{3}} + \tfrac{1}{4}(3-k). \tag{8}$$

On turning now to the momentum equation, this takes the non-dimensional form

$$w^* = \frac{1-\beta}{\beta+k}, \quad \text{where} \quad w^* = w\frac{H_0}{h_2 I_0}.$$

This can be expressed in differential form as

$$\frac{dz^*}{dt^*} = \frac{1}{(1+k)x+k}, \tag{9}$$

the quantity z^* being the non-dimensional distance travelled by the centre of gravity of the element. Equations (7) and (9) can be used to derive the following relationship between z^* and x:

$$\frac{dz^*}{dx} = \frac{1}{3\alpha(1+x)^{\frac{2}{3}}},$$

which integrates to

$$1+\alpha z^* = (1+x)^{\frac{1}{3}}.$$

From the definition of x and (6), we obtain

$$b^* = 1+\alpha z^*, \tag{10}$$

and the successive outlines of the puff map out a truncated cone of half-angle $\tan^{-1}\alpha$ at all times. Putting $k = \frac{1}{2}$, the value appropriate to a sphere, the motion is described by the following non-dimensional equations:

$$\alpha t^* = \tfrac{3}{8}(1+\alpha z^*)^4 - (1+\alpha z^*) + \tfrac{5}{8}, \tag{11}$$

$$w^* = \frac{2}{3(1+\alpha z^*)^3 - 2}. \tag{12}$$

Figure 4 shows the solution of (11) together with the short- and long-time asymptotes. The puff starts with unit radius and an initial velocity $w^* = 2$, all the momentum residing in the external fluid; at long times the motion approaches the asymptotic condition

$$\alpha t^* = \tfrac{3}{8}(\alpha z^*)^4. \tag{13}$$

The corresponding equations for a 2-dimensional puff are

$$\alpha t^* = \tfrac{2}{3}(1+\alpha z^*)^3 - (1+\alpha z^*) + \tfrac{1}{3}, \tag{14}$$

$$w^* = \frac{1}{2(1+\alpha z^*)^2 - 1}, \tag{15}$$

and for long times

$$\alpha t^* = \tfrac{2}{3}(\alpha z^*)^3. \tag{16}$$

4. Measured puff behaviour

Tests were performed on the plasma jet over a range of initial stored energies from 0.5 to 5 J with discharge times of between 8 and 40 μs to current maximum. Although the discharge times are small compared with the life times of the observed turbulent puffs, the rate at which the energy was introduced had a considerable influence on the mixing configuration during the early times of observation, ranging in appearance from a well-formed isolated 'puff' to a shape reminiscent of the starting plume (Turner 1973). In general, the form of the mixing region evolved with time, and for the present experiments discharge conditions were chosen that minimized these changes in form, conditions that coincidentally had been used for combustion studies. Results will be described from two sets of discharge conditions: 15 μF at 800 V and 4 μF at 700 V, providing 4.8 and 0.98 J of stored energy respectively.

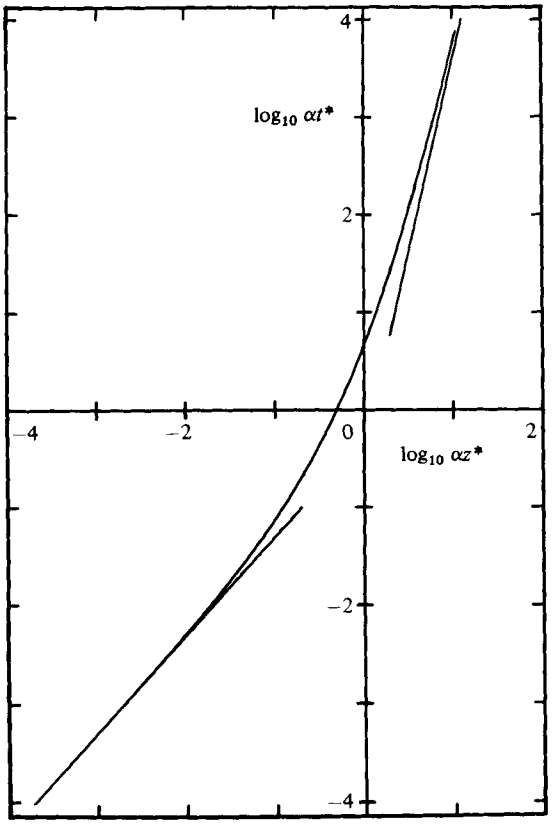

FIGURE 4. Idealized non-buoyant puff solution (11).

The events were photographed with a Fastax high-speed ciné camera running at about 4000 frames per second using a double-pass schlieren system to record the evolution of the mass of heated gas. Separate experiments were performed to determine the total energy and momentum imparted to the gas and also to measure the temperature within the puff at various distances from the cavity exit. Since these sets of measurements were carried out independently, and the results obtained as averages of many events, we do not have a complete description of any one event, but nevertheless the measurements do provide a background against which the scaling laws can be tested.

The actual energy introduced into the gas was measured by discharging the device into a closed volume and measuring the resulting pressure rise, the apparatus used being similar to that described by Smy *et al.* (1983). The conditions for stored energies of 4.8 and 0.98 J yielded values of M_0 of 0.288 and 0.088 J respectively, these figures being averages of about 10 events, with a scatter of $\pm 10\,\%$. The low proportion of the stored energy actually imparted to the gas is typical of such devices; see for example Smy *et al.* (1983) and Carleton, Vince & Weinberg (1982) for further examples. Most of the energy is absorbed in electrical-resistance losses and in the arc anode and cathode voltage drops.

To measure the total momentum imparted to the gas, the discharge chamber was mounted on an enclosed pendulum with the current supply led via mercury-pool contacts. The firing of the discharge was synchronized to the pendulum motion so

that the momentum imparted by the device was summed over many events. The momentum added was deduced by comparing the damping rate of the pendulum with and without the plasma jet firing, by means of a mirror attached to the apparatus and a simple light lever. It was found that more-consistent results were obtained by increasing the decay rate with magnetic damping rather than relying on atmospheric and bearing friction (D. Simeoni 1983 private communication). Any possible effects of electromagnetically induced torques were assessed by replacing the discharge path by a direct circuit: no effect could be detected. The stored energies of 4.8 and 0.98 J imparted total impulses of 2.26×10^{-5} and 1.2×10^{-5} kg m/s respectively, these being averages of about 100 events each. The repeatability of successive sets of measurements was $\pm 5\,\%$.

The density changes within the puff were measured as they traversed an optical probe placed at known distances from the cavity exit. Light from a laser interferometer was led into the path of the puff along a pair of opposing hypodermic needles, the separation between the ends of the needles defining a cylindrical measurement volume about 1 mm long and 1 mm in diameter. Changes in fringe position were sensed with a photodiode and fed to an oscilloscope which gave a record of the variation of density at a point as the puff passed the probe. As might be expected, the individual measurements had a large scatter, as the temperature is a function of the puff expansion angle and the point within the puff. The system is described in greater detail by Clements *et al.* (1983).

The ciné films were analysed by digitizing the position of the advancing front and the extremes of the puff in a direction normal to the motion. As can be seen in the example shown in figure 3, the shape of the heated gas changed from conical at the instant the discharge ceased to roughly spherical after about 5 ms. Single-frame photographs confirmed the symmetry about the direction of travel. A certain amount of subjective judgement was exercised in the analysis of the early frames, as often only a part of the ejected gas evolved to the spherical form, the remainder forming a 'wake' region or trail. In these cases, specific features on the outer edges of the final form were identified and their positions followed back to earlier times. Figure 3(*b*) shows such an example, whilst 3(*c*) has a more clearly defined structure. Figure 3(*a*) is an example of a rather irregular formation which was discarded from the analysis. At long times when the density differences become small, the radial extent of the heated gas can no longer be discerned, although the advancing frontal region can be followed to rather longer times. This introduces a certain bias into the interpretation of the behaviour which will be discussed later.

Figure 5 shows a typical example of the digitized data, and is a plot of the maximum half-width of the puff against the position of the advancing front. The puff appears to expand rapidly at first, with a rather abrupt transition to a low expansion rate at long times. The corresponding curves of the position of the advancing front as a function of time show no such sudden changes, however. A close examination of the films revealed that the apparent decrease in expansion angle arose from a change in geometry rather than a reduction in the rate of volume increase. It is clear, perhaps not surprisingly, that these are not exactly self-preserving flows. To enable a comparison to be made with the theory of §3, the actual puff shapes have been replaced by equivalent spherical elements having roughly the same volumes. This was done for a few selected frames from each film, equivalent sphere radii were calculated and the corresponding front positions calculated from a polynomial curve fitted to the front-position–time data. The resulting points are shown on figure 5 for comparison with the actual width measurements. The volume-averaged radii give a more

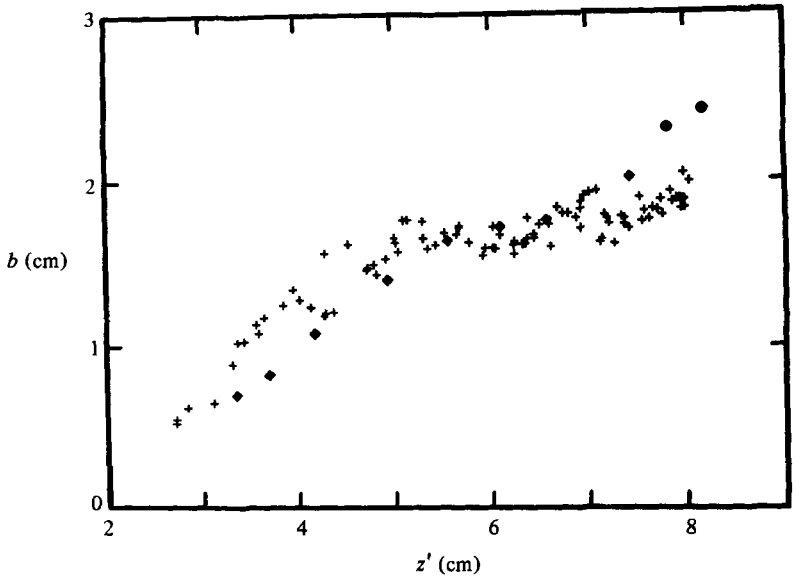

FIGURE 5. Maximum half-width of puff as a function of maximum penetration distance: +, digitized points; ◆, equivalent spherical radius.

linear expansion, and these have therefore been used to define values of the parameter α for each experiment. Figure 6 summarizes the linear fits to the equivalent spherical radii for all eight sets of data.

To reduce z', the measured position of the front of the element, to z, the position of the centre of the sphere from the origin defined in the model, three corrections must be made. The apparent position z_0 of the apex of the conical expansion, the distance z_1 from the apex to the point at which the non-dimensional radius is unity, and the equivalent spherical radius b must all be subtracted. In symbolic form

$$z = z' - z_0 - z_1 - b,$$

where

$$z_1 = \frac{1}{\alpha}\left(\frac{3H_0}{4\pi\rho_2 h_2}\right)^{\frac{1}{3}}, \quad b = \alpha(z+z_1),$$

giving

$$z = \frac{z'-z_0}{1+\alpha} - \frac{1}{\alpha}\left(\frac{3H_0}{4\pi\rho_2 h_2}\right)^{\frac{1}{3}}.$$

Figures 7 and 8 show plots of the time as a function of the fourth power of the corrected axial distance z for the low- and high-energy experiments, the corresponding values of α being listed in table 1. These plots are expected to tend towards linearity at long times (see (A 1) in the Appendix). Figures 9–11 show the results in non-dimensional form as αt^* as a function of $(\alpha z^*)^4$. There is no well-defined time origin for the experimental results in this form, since the origin of the distance coordinate z has been defined on the basis of a self-preserving flow approximation to the true behaviour. The times for each experiment have been adjusted to correspond to zero at $z = 0$; as can be seen, the sets of points from the different experiments are brought to near-coincidence.

Figure 9 shows the results of the low-energy conditions, where it can be seen that, compared with the unscaled results of figure 7, the scaling has afforded a reasonable

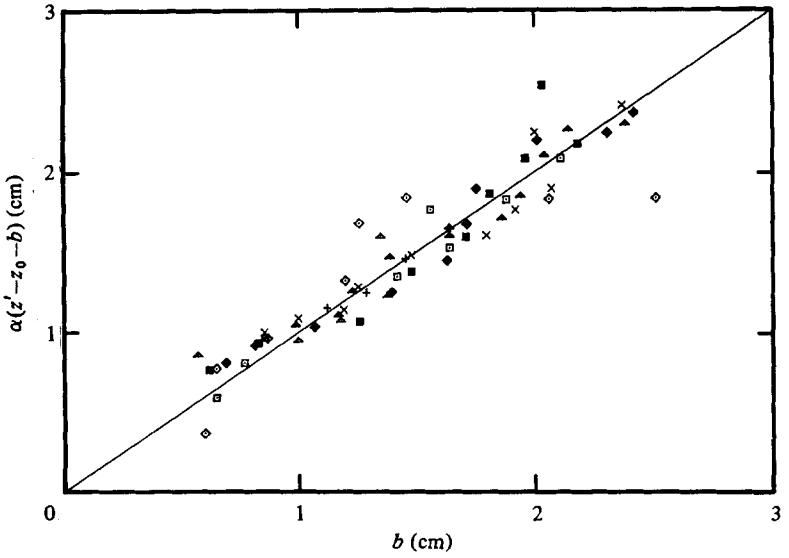

FIGURE 6. Linear fit of equivalent spherical radii to position of sphere centre; symbols as as in table 1.

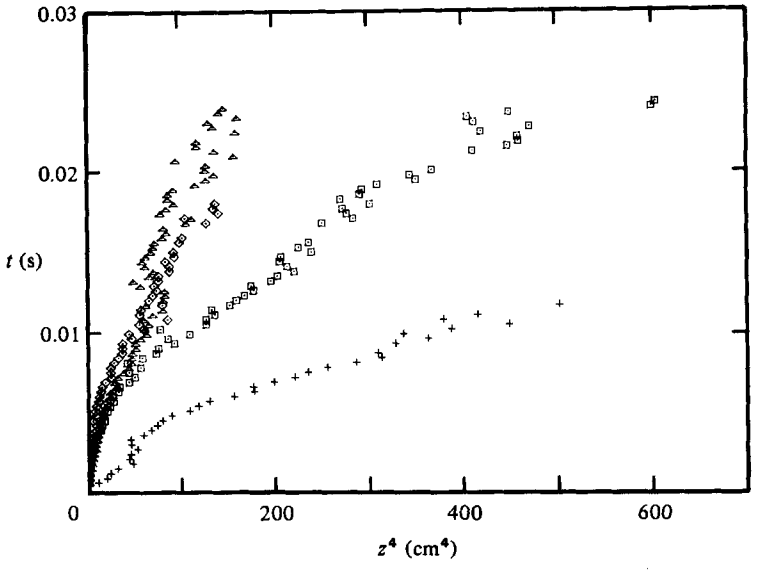

FIGURE 7. Time as a function of the fourth power of the corrected axial distance z for the low-energy results; symbols as in table 1.

collapse of the data. Figure 10 shows the results of the high-energy experiments, and a similar collapse of the data is obtained. It should be noted that the scaling has condensed the high-energy results to a small proportion of the range covered by the low-energy results, even though they extend over greater distances in real space.

For comparison, figure 11 shows a portion of the low-energy results to the same scale, and, apart from an offset in the timescales, the results from the two different energy conditions give very similar curves.

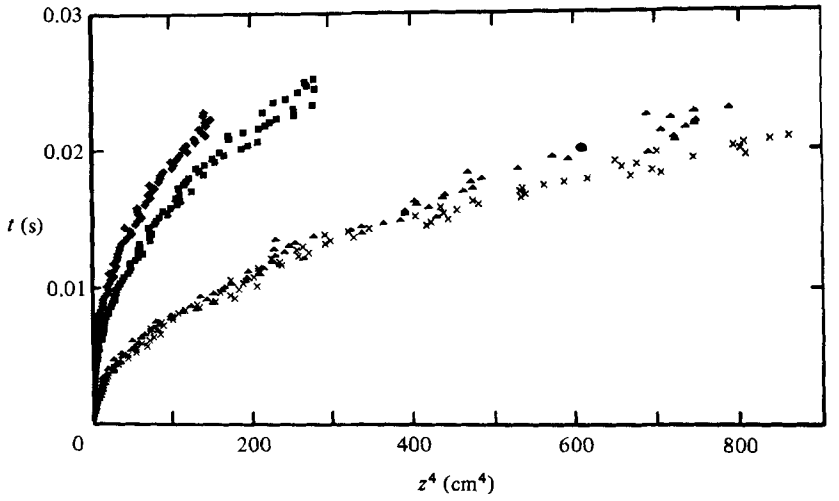

FIGURE 8. Time as a function of the fourth power of the corrected axial distance z for the high-energy results; symbols as in table 1.

Run no.	Stored energy (J)	Symbol	α	z_0 (cm)	t_0 (ms)
1	0.98	□	0.363	−0.027	−3.0
2	0.98	◇	0.498	0.559	−2.0
3	0.98	△	0.598	−0.554	−4.0
4	0.98	+	0.276	−3.379	−6.0
5	4.8	■	0.453	2.965	0.0
6	4.8	●	0.503	1.056	0.7
7	4.8	▲	0.327	−0.348	−6.0
8	4.8	×	0.337	−0.743	−6.0

TABLE 1. Conditions and parameters of the experimental data

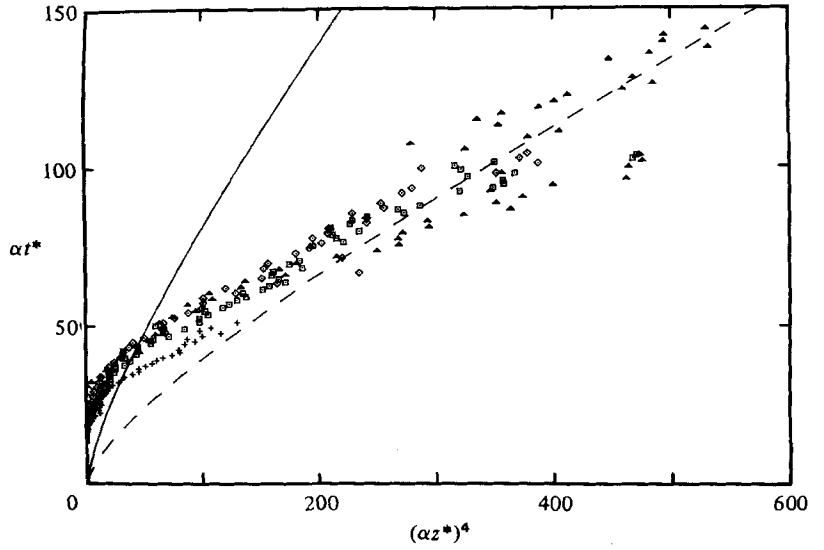

FIGURE 9. Non-dimensional presentation of the low-energy, symbols as in table 1; ——, theory adjusted to be asymptotic to Richards' (1965) result $C_3 = 0.33$; – – –, $C_3 = 0.85$.

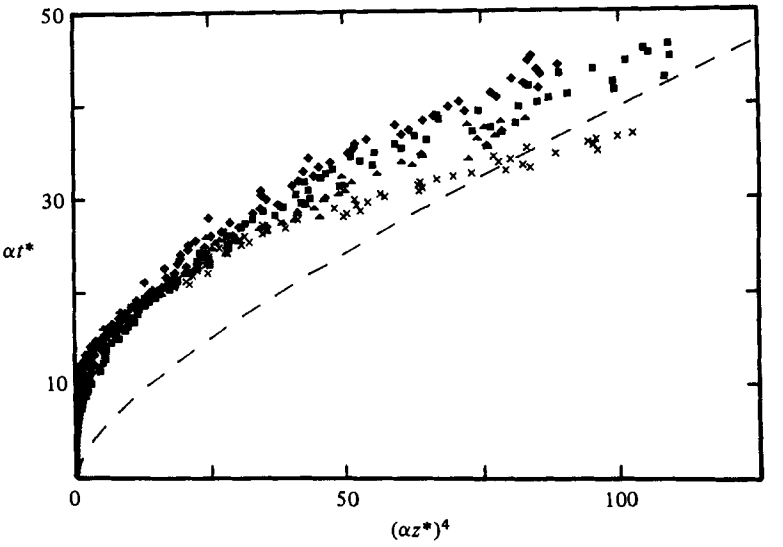

FIGURE 10. Non-dimensional presentation of the high-energy results; symbols as in table 1; – – –, $C_3 = 0.85$.

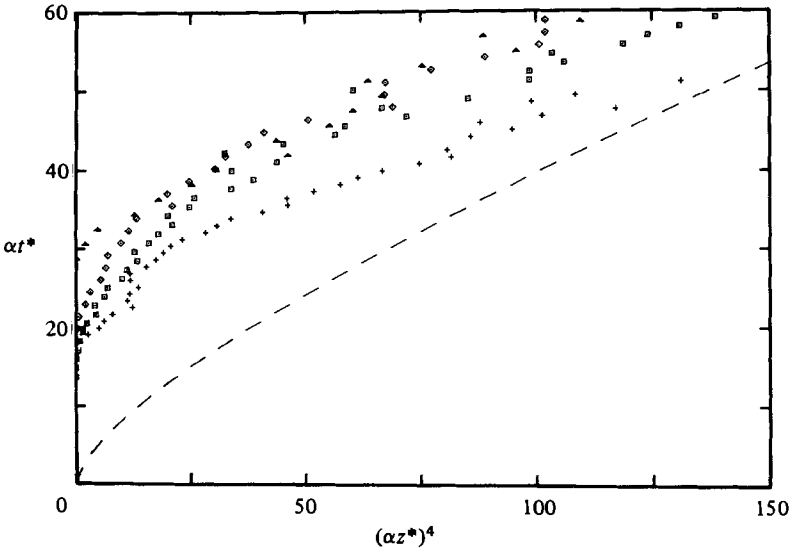

FIGURE 11. Non-dimensional presentation of the low-energy results to the same scale as figure 10.

Table 2 lists the temperature measurements, and in each case the result is an estimate of the mean puff temperature averaged over many shots. The results are shown in figure 12, with the parameter $1-\beta$ plotted as a function of αt^*, and the two sets are consistent with the predicted scaling. Figure 13 shows a typical oscilloscope trace of the interferometer output.

Stored energy (J)	Time (ms)	ΔT (°C)
0.98	2	40
0.98	4	14
0.98	5	14
0.98	9	10
4.8	0.4	400
4.8	1.5	120
4.8	5.0	30
4.8	7.0	20
4.8	12.0	14
4.8	20.0	7

TABLE 2. Measured mean puff temperature above ambient temperature

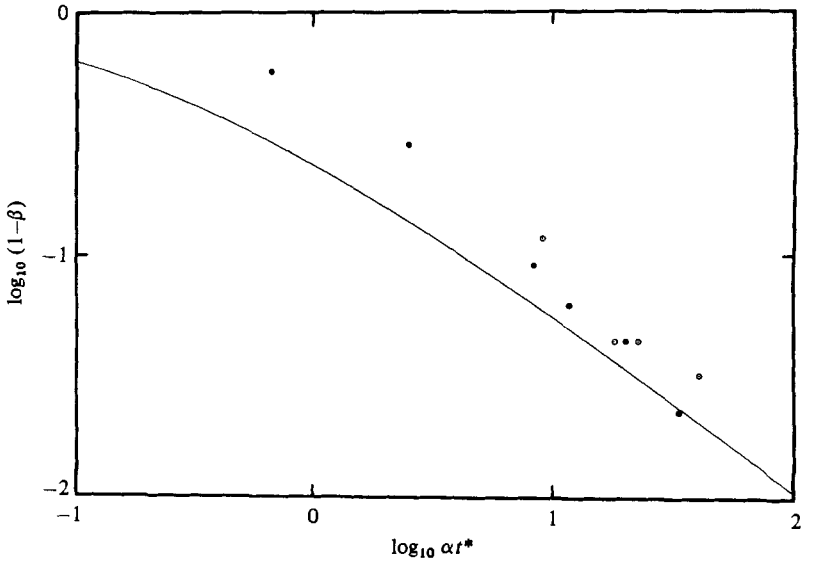

FIGURE 12. Non-dimensional presentation of density measurements; ○, low-energy results; ●, high-energy results.

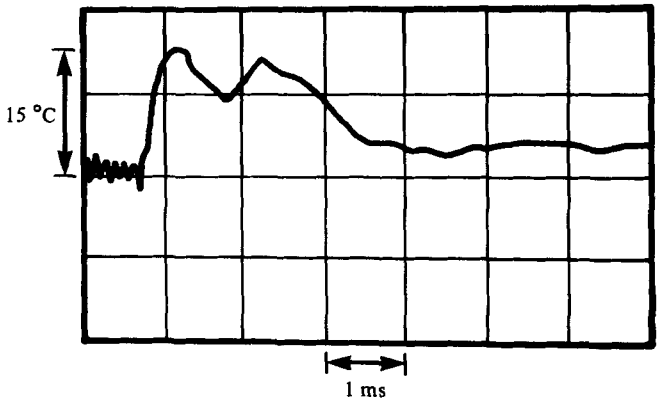

FIGURE 13. Tracing of a typical oscilloscope trace of the interferometer output.

5. Discussion

Two distinct mixing phases for the dilution of the plasma-jet exhaust are suggested by our results. First, during the electrical discharge, the density differences in the flow give rise to high rates of shear as the jet penetrates into the quiescent ambient fluid. Laser schlieren photographs taken during this period give the appearance of a turbulent mixing zone, confirmed by still photographs of the outer portions of the luminous region, which exhibit eddy structures typical of an entraining flow. Although we have no other direct evidence, the high overall Reynolds numbers during this phase, of order 10^4, suggest that turbulence plays an important role in the formation of these structures.

After the cessation of the discharge, the mass of heated gas evolves from its initial conical shape to an approximately spherical turbulent element. The major part of this transition is completed within about 5 ms, although not all the fluid ejected is incorporated into the spherical element during this time, some remaining as a wake or 'tail'. At later times the turbulent element grows in an approximately similar geometrical pattern. The departures from true similarity generally take the following form: the element at first is rather flattened in its direction of motion, and at later times becomes more spherical, and during this transition period fluid accumulates at the rear of the element in preference to the radial direction. At this time the element is entraining fluid that originally formed the 'wake' or tail in the earlier formation stages. This fluid has associated with it some of the thermal energy and momentum originally imparted to the gas within the cavity. Our optical system did not have the sensitivity to follow the motion long enough to determine the ultimate form of our elements.

The model results of (11) are shown as the solid line on figure 9, with the coefficients adjusted to match the asymptotic solution to Richards' (1965) empirical results for the neutral density puff (see the Appendix). There is a large discrepancy between this calculated curve and the experimental results, and the following possible explanations are offered. First, in fitting a mean value of α to a given set of results, a bias towards earlier times is introduced, since the inferior resolution of the photographs in the transverse direction limits the time over which the expansion rate can be determined, whereas the frontal position could be followed for much longer times. Thus the mean value of α used in the scaling may be larger than is appropriate for the longer times, as the actual puff behaviour is not exactly self-preserving and there is a tendency for the expansion rate to decrease with time. Secondly, the internal structure may differ from Richards' case, and the value of 0.33 for the constant C_3 may not be appropriate.

The representation of the results in the form chosen for figures 9–11 is rather sensitive to changes in the parameter α, and as an example the dotted curve running parallel to the experimental points has been drawn by changing the scales of the theoretical curve to simulate the effect of reducing α to 75 % of the measured values. Such a reduction is in keeping with the observed departures from similarity. By way of contrast, an increase in the value of C_3 from 0.33 to 0.85 is required if this alone is the reason for the mismatch between theory and experiment.

The view that the discrepancy arises from inappropriate values of α is reinforced if the measured and calculated densities are compared. This is shown on figure 12, and with this presentation the sensitivity of the theory to changes in the values of α and C_3 is the same. The curve is the theoretical solution, scaled to account for a 25 % reduction in α. The measurements follow the trend indicated by the theory,

Experiment	α	t_c (s)	V_c (m/s)
Plasma-jet puffs	0.4	0.004	20
Metal particles/water	0.25	0.02	2.0
High-energy detonation	0.1	3	30
Trinity explosion	0.1	15	150

TABLE 3. Comparison of plasma-jet parameters with related phenomena

although the points lie somewhat above the curve. If, however, the theoretical curve is plotted with C_3 set to 0.85 instead of 0.33, a very large discrepancy is introduced. Thus it is only possible to reconcile the theoretical results with the measurements of both puff position and density by slightly reducing the estimates of α at longer times.

A third source of departure of the model from reality is the loss of fluid to a wake. In the early stages our division of the fluid into 'puff' and wake is somewhat arbitrary, and, as at least some of this residual fluid is later incorporated into the rear of the puff, it is difficult to assess the overall effect. It is possible, however, to estimate the expected loss of impulse to the wake over larger times if, following Escoudier & Maxworthy (1973), a drag coefficient is defined and the loss of impulse determined by integration over the time of interest. The loss of impulse ΔI_0 can thus be written as

$$\Delta I_0 = \int_0^t \tfrac{1}{2} C_D \pi b^2 w^2 \, \mathrm{d}t.$$

Taking C_D from Escoudier & Maxworthy (1973) in the range 10^{-1}–10^{-2} and estimating the integral from the measured puff yields a change in impulse pulse in the range 10^{-6}–10^{-7} kg m/s over 20 ms, compared with the measured total impulse of order 10^{-5} kg m/s. Thus over the later stages of the observation period the wake losses are not severe.

The detailed behaviour of our turbulent elements clearly violates some of our assumptions, viz. those of no wake and of exactly self-preserving development, but nevertheless the results are correlated well by parameters based on the similarity analysis. We feel that, in spite of these shortcomings, the self-preserving entrainment formulation provides a useful framework for the discussion of parameters controlling the ignition characteristics of such devices.

Our present results occupy a range of characteristic time and velocity scales unexplored by previous work, as can be seen by a comparison with those of related phenomena, taken here from table 1 of Escoudier & Maxworthy and displayed in table 3. It can be seen that our timescales are an order of magnitude shorter than other short-timescale work, principally on very heavy thermals, but that the velocity scales are typical of high-energy explosions.

Appendix

It is interesting to compare the dimensional form of the long-time asymptotic solutions for the spherical and cylindrical cases with those derived by Richards (1965). The long-time solutions of (13) and (16) take the dimensional forms

$$(\alpha z)^3 = \frac{3}{2\pi}\frac{I_0 \alpha t}{\rho_2}, \quad (\alpha z)^4 = \frac{2}{\pi}\frac{I_0 \alpha t}{\rho_2} \tag{A 1}$$

for the two- and three-dimensional cases respectively.

The corresponding solutions in Richards' formulation are

$$\left(\frac{z'}{n}\right)^3 = 3C_2\frac{I_0}{\rho_2}\frac{t}{n}, \quad \left(\frac{z'}{n}\right)^4 = 4C_3\frac{I_0}{\rho_2}\frac{t}{n}, \tag{A 2}$$

where z' is the position of the leading edge of the puff and n is the ratio z'/b. The parameters n and α are thus related geometrically by

$$\alpha = \frac{1}{n-1}.$$

Noting that $\alpha z = z'/n$, both being by definition the radius, (A 1) can be recast in Richards' notation as

$$\left(\frac{z'}{n}\right)^3 = \frac{3}{2\pi}\frac{n}{n-1}\frac{I_0}{\rho_2}\frac{t}{n}, \quad \left(\frac{z'}{n}\right)^4 = \frac{2}{\pi}\frac{n}{n-1}\frac{I_0}{\rho_2}\frac{t}{n}.$$

Comparing these with Richard's relationships (A 2) gives

$$C_2 = C_3 = \frac{1}{2\pi}\frac{n}{n-1}.$$

The mean values of n for Richards spherical and cylindrical experiments were 3.5 and 4.5 respectively, yielding

$$C_2 = 0.20, \quad C_3 = 0.22,$$

compared with Richards empirical values of $C_2 = 0.27$ and $C_3 = 0.33$. Thus the asymptotic form of our solutions is at least compatible with Richards, experimental findings.

The authors would like to acknowledge the assistance of D. Way-Nee, D. Ridley and J. Anglehart, as well as the financial assistance of the Natural Sciences and Engineering Research Council of Canada. We would also like to extend our thanks to Professor B. R. Morton for taking the time to discuss this problem with us during a recent visit to the Institute of Ocean Sciences.

REFERENCES

Carleton, F. B., Vince, I. M. & Weinberg, F. J. 1982 Energy and radical losses from plasma jet igniters to solid surfaces. In *Proc. 19th Symp. (Intl) on Combustion*, pp. 1523–1531. Combustion Institute.

Cetegen, B., Teichman, K. Y., Weihberg, F. J. & Oppenheim, A. K. 1980 Performance of a plasma jet igniter. *SAE Paper* 800042.

Clements, R. M., Smy, P. R & Dale, J. D. 1981 An experimental study of the ejection mechanism for typical plasma jet igniters. *Combust. Flame* **42**, 287–295.

Clements, R. M., Smy, P. R., Topham, D., Vince, I. M., Vovelle, C. & Weinberg, F. J. 1983 Chemical activity and transport processes in the vicinity of a plasma jet igniter. *Combust. Flame* (submitted).

Escudier, M. P. & Maxworthy, T. 1973 On the motion of thermals. *J. Fluid Mech.* **61**, 541–552.

Grant, J. F., Marram, E. P. & McIlwain, M. E. 1983 Optimization of plasma jet ignition properties: ignition of lean-quiescent mixtures of propane. *Combust. Sci. Tech.* **30**, 171–184.

Grigg, H. R. & Stewart, R. W. 1963 Turbulent diffusion in a stratified fluid. *J. Fluid Mech.* **15**, 174–186.

Hopkins, D. F. & Robertson, J. M. 1967 Two-dimensional incompressible fluid jet penetration. *J. Fluid Mech.* **29**, 273–287.

MORTON, B. R., TAYLOR, G. I. & TURNER, J. S. 1956 Turbulent gravitational convection from maintained and instantaneous sources. *Proc. R. Soc. Lond.* A **234**, 1–23.

OVED, Y., MILLINAZZO, F., CLEMENTS, R. M. & SMY, P. R. 1979 Blast waves produced by a time-dependent energy source. *AIAA J.* **17**, 601–605.

RICHARDS, J. M. 1965 Puff motions in unstratified surroundings. *J. Fluid Mech.* **21**, 97–106.

SCORER, R. S. 1978 *Environmental Aerodynamics*. Wiley.

SMY, P. R., CLEMENTS, R. M., SIMEONI, D. & TOPHAM, D. R. 1982 Plasma expulsion from the plasma jet igniter. *J. Phys.* D: *Appl. Phys.* **15**, 2227–2239.

SMY, P. R., CLEMENTS, R. M., DALE, J. D., SIMEONI, D. & TOPHAM, D. R. 1983 Efficiency and erosion characteristics of plasma jet igniters. *J. Phys.* D: *Appl. Phys.* **16**, 783–791.

TOPHAM, D. R., SMY, P. R. & CLEMENTS, R. M. 1975 An investigation of a coaxial spark igniter with emphasis on its practical use. *Combust. Flame* **25**, 187–195.

TOPHAM, D. R., ZHANG, J. X., CLEMENTS, R. M. & SMY, P. R. 1982 Turbulent mixing induced by a high-energy ignition device. *J. Phys.* D: *Appl. Phys.* **15**, L65–67.

TURNER, J. S. 1964 The flow into an expanding spherical vortex. *J. Fluid Mech.* **18**, 195–208.

TURNER, J. S. 1973 *Buoyancy Effects in Fluids*. Cambridge University Press.

ZHANG, J. X., CLEMENTS, R. M. & SMY, P. R. 1983 An experimental investigation of the effect of a plasma jet on a freely expanding methane–air flame. *Combust. Flame* **50**, 99–106.